Journal of Materials Chemistry A

ROYAL SOCIETY OF CHEMISTRY

PAPER

View Article Online
View Journal | View Issue

Cite this: J. Mater. Chem. A, 2026, 14, 13874

Carbon tetrafluoride – sulphur hexafluoride adsorption and separation with zirconium metal–organic frameworks decorated with fluorinated thiazolium salts

Giacomo Provinciali, [a] Giulio Bicchierai, [a] Zhi Fang, [b] Tongan Yan, *[c] Lorenzo Donà, *[d] Bartolomeo Civalleri, [d] Hongliang Huang, [c] Giuliano Giambastiani, [efa] Giulia Tuci [af] and Andrea Rossin *[af]

The 8-connected fully-carbocyclic zirconium MOF $[Zr_6O_4(OH)_6(H_2O)_2(HCOO)_2(TCPB)_2]$ [**Zr_TCPB**, H_4TCPB = 1,2,4,5-tetrakis(4-carboxyphenyl)benzene] has been post-synthetically decorated with the two F-containing thiazolium salts 3-(4-carboxy-2-fluorobenzyl)thiazol-3-ium bromide [**(HPhTz^{F})Br**] and 3-(4-carboxy-2-(trifluoromethyl)benzyl)thiazol-3-ium bromide [**(HPhTz^{CF3})Br**] *via* Solvent-Assisted Ligand Incorporation (SALI). After salt anchorage to the metal nodes through their carboxylic function and concomitant water elimination (condensation), two mixed-linker MOFs of general formulae $[Zr_6O_4(OH)_5(H_2O)(HCOO)_2(TCPB)_2(PhTz^{F})]Br$ (**Zr_TCPB_F**) and $[Zr_6O_4(OH)_5(H_2O)(HCOO)_2(TCPB)_2(PhTz^{CF3})]Br$ (**Zr_TCPB_CF3**) have been obtained. They have been fully characterized in the solid-state and exploited as functional materials for SF_6 and CF_4 adsorption. The introduction of an F-containing moiety in the pristine MOF improves the fluorinated gas thermodynamic affinity, as witnessed by the increased SF_6 and CF_4 adsorption enthalpies (Q_{st}) of **Zr_TCPB_F** and **Zr_TCPB_CF3** in comparison to those of bare **Zr_TCPB**. Intriguingly, the replacement of a simple fluoro (–F) substituent with a trifluoromethyl ($-CF_3$) group on the thiazolium salt switches the MOF preferential adsorption from SF_6 to CF_4. This behavior is unprecedented to our knowledge, opening new horizons in the discrimination of fluorinated polluting gases in the field of air treatment and cleaning. Both MOFs are selective toward SF_6 in SF_6/CF_4 equimolar binary mixtures, because of the higher SF_6 polarizability (due to the much larger and more diffuse central sulfur atom) that translates into stronger dispersion (van der Waals) interactions with the MOFs. The best performance has been found for **Zr_TCPB_CF3** (with $S_{SF6/CF4} = 9$). Therefore, both materials can be exploited in fluorinated gas separation as further demonstrated by periodic DFT calculations carried out on model systems.

Received 18th December 2025
Accepted 24th February 2026

DOI: 10.1039/d5ta10343f

rsc.li/materials-a

1 Introduction

Air pollution, driven by a variety of human activities, continues to pose a major threat to both environmental health and climate stability. Among the lesser-known but highly impactful pollutants are fluorinated greenhouse gases, that contribute approximately 2% of the global greenhouse gas emissions.[1,2] The rapidly increasing demand for refrigeration and cooling services, particularly in developing countries, threatens to increase fluorinated gas emissions considerably over the next few decades. Two important members of this family are carbon tetrafluoride (CF_4) and sulfur hexafluoride (SF_6). These gases [although present in much lower environmental concentrations in the order of parts per trillion (ppt) compared to carbon dioxide (CO_2)] have an extremely high global warming potential (GWP) because, for a given amount of mass, they trap substantially more heat than CO_2 and can persist in the atmosphere for hundreds to thousands of years, contributing to the greenhouse effect.[3] CF_4 is primarily used in the semiconductor industry, where it is employed as a plasma etching gas during the production of microchips. It is also used in the production of aluminum and as a refrigerant in certain niche applications. Its chemical inertness and stability make it an ideal compound for these high-tech processes, but this also means that once

[a]Istituto di Chimica dei Composti Organometallici (CNR-ICCOM), Via Madonna del Piano 10, Sesto Fiorentino, Firenze, 50019, Italy. E-mail: andrea.rossin@cnr.it
[b]School of Materials Science and Engineering, Tiangong University, Tianjin 300387, China
[c]School of Chemistry and Chemical Engineering, Tiangong University, Tianjin 300387, China. E-mail: yantongan@tiangong.edu.cn
[d]Department of Chemistry, NIS and INSTM Reference Centre, Università di Torino, Via G. Quarello 15, 10135 and Via P. Giuria 7, 10125 Torino, Italy. E-mail: lorenzo.dona@unito.it
[e]Dipartimento di Chimica "Ugo Schiff", Università di Firenze, Via della Lastruccia 3-13, 50019 Sesto Fiorentino, Firenze, Italy
[f]Consorzio Interuniversitario Nazionale per la Scienza e Tecnologia dei Materiali (INSTM), Via G. Giusti, 9 50121, Firenze, Italy

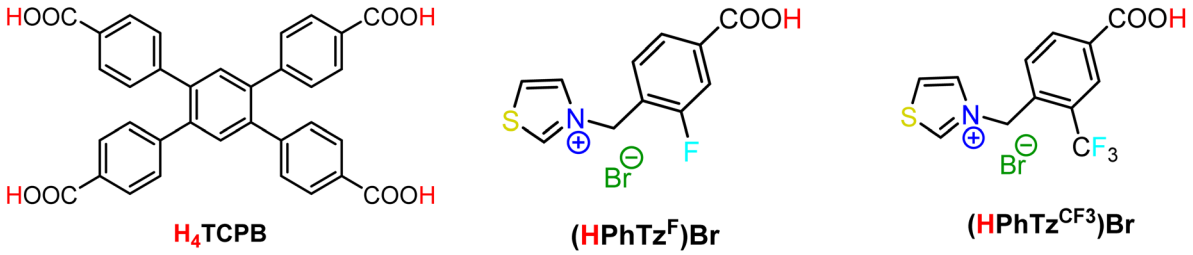

Scheme 1 The linkers used in this study for the construction of the Zr^{IV} MIXMOFs **Zr_TCPB_F** and **Zr_TCPB_CF3**: 1,2,4,5-tetrakis(4-carboxyphenyl)benzene (H_4TCPB), 3-(4-carboxy-2-fluorobenzyl)thiazol-3-ium bromide [**(HPhTz^{F})Br**] and 3-(4-carboxy-2-(trifluoromethyl)benzyl) thiazol-3-ium bromide [**(HPhTz^{CF3})Br**].

released, CF_4 persists in the atmosphere for centuries.[4–6] SF_6 is widely used as an insulating gas in high-voltage electrical equipment, such as circuit breakers, switchgear, and transformers, due to its excellent dielectric properties. It is also used in particle accelerators and medical devices like MRI machines. The chemical stability and insulating qualities of SF_6 make it invaluable in these applications, ensuring reliable and efficient operation of equipment that powers critical infrastructure. However, the use of SF_6 in these industries has raised concerns due to its extremely high GWP, which is over 22 000 times greater than CO_2 on a per molecule basis.[7–9] Small atmospheric concentrations of these two gases can have large effects on global temperatures. Thus, controlling and mitigating their release into the environment has become a critical objective for reducing the overall carbon footprint and achieving international climate goals, including those set out in the Paris Agreement.[10] Metal–organic frameworks (MOFs), with their unique structural characteristics, have emerged as promising candidates for addressing this issue due to their exceptional surface area, tunable porosity, and chemical versatility.[11–14] MOFs are typically composed of metal clusters linked by organic ligands, allowing for the precise design of pore structures that can selectively adsorb and separate specific gases. This adaptability makes MOFs a compelling solution for the selective capture of gases such as fluorinated compounds, which require highly specialized materials for effective separation. Given the strong C–F and S–F bonds in CF_4 and SF_6, their adsorption requires MOFs with tailored pore environments and strong host-guest interactions.[15–18] MOFs containing open metal sites, fluorophilic functional groups, or optimized pore dimensions have demonstrated enhanced uptake of these gases. Additionally, post-synthetic modifications and functionalized ligands can further improve adsorption performance.[19–25] In recent years, the incorporation of fluorine into the structure of MOFs has opened new avenues for enhancing their performance in gas separation applications. Fluorine, with its strong electronegativity, can contribute to the stabilization of metal centers and introduce additional functionalities to the material. Fluorinated MOFs in particular offer advantages, such as increased chemical stability and enhanced interactions with fluorinated gases. These unique properties enable these materials to act as highly efficient adsorbents, capable of selectively capturing and separating fluorinated compounds from complex gas mixtures.[26–28] In the semiconductor industry, CF_4 and SF_6 mixtures are used in plasma etching processes for the fabrication of integrated circuits. These mixtures allow precise control of the etching, thanks to their chemical properties and the ability to form reactive plasmas. After use, exhaust gases may contain reactive or incompletely dissociated residues. Separating CF_4 from SF_6 allows the recovery and reuse of gases, the reduction of the load on scrubber systems and the improvement of process efficiency. SF_6/CF_4 mixtures are also exploited in gas-insulated switchgears in low-temperature environments, such as arctic regions. The addition of CF_4 to SF_6 prevents condensation of SF_6 at temperatures below 233 K, maintaining insulating properties and ensuring reliable operation. During maintenance or emptying of the system, it is necessary to separate the two components to optimize recycling, to avoid contamination and to restore the original mixture in a controlled manner. Given the growing concerns over the environmental impact of fluorinated gases, the development of fluorine-containing MOFs for their selective adsorption/separation has the potential to play a key role in mitigating their release into the atmosphere. The introduction of fluorinated linkers in a MOF can be accomplished either *via* direct synthesis under solvothermal conditions or *via* post-synthetic modification through the reaction known as Solvent-Assisted Ligand Incorporation (SALI).[29–32] Recent work of our group has exploited the latter approach for the construction of mixed-linker MOFs (MIXMOFs) decorated with thiazole-based organic groups for assorted applications, spanning from CO_2 capture to luminescence sensing of wastewater contaminants.[33–36] Following this research interest and with the fluorinated gas adsorption/separation application in mind, we have prepared two new F-containing monocarboxylic thiazolium salts **(HPhTz^{F})Br** and **(HPhTz^{CF3})Br** (Scheme 1). Subsequently, we have decorated the 8-connected zirconium MOF $[Zr_6O_4(OH)_6(H_2O)_2(HCOO)_2(TCPB)_2]$ (H_4TCPB = 1,2,4,5-tetrakis(4-carboxyphenyl)benzene, Scheme 1, **Zr_TCPB**] with these salts using SALI. The as-obtained MIXMOFs after water elimination with minimal formulae $[Zr_6O_4(OH)_5(H_2O)(HCOO)_2(TCPB)_2(\mathbf{PhTz^{F}})]Br$ (**Zr_TCPB_F**) and $[Zr_6O_4(OH)_5(H_2O)(HCOO)_2(TCPB)_2(\mathbf{PhTz^{CF3}})]Br$ (**Zr_TCPB_CF3**) have been fully characterized in the solid-state and exploited as functional materials for SF_6 and CF_4 adsorption.

2 Experimental section

2.1 Materials and methods

Zirconium chloride ($ZrCl_4$, Sigma Aldrich), formic acid (HCOOH, Sigma Aldrich), *N*,*N*-dimethylformamide (DMF, Sigma Aldrich) and H_2TCPB (Sigma Aldrich) were purchased from commercial vendors and used as received. **Zr_TCPB** was prepared according to the synthesis reported by Farha *et al.* in 2019.[37] The preparation and characterization of [**(HPhTz^{F})Br**] and [**(HPhTz^{CF3})Br**] is reported in the SI (Fig. S1, S2, Tables S1 and S2). NMR spectra were recorded on BRUKER AVANCE 400/600 MHz spectrometers, with chemical shifts (δ) reported in parts per million (ppm) downfield of tetramethylsilane (TMS, ^{1}H, ^{13}C) or trichlorofluoromethane ($CFCl_3$, ^{19}F) and calibrated against the residual protiated solvent resonance. FT-IR spectra (KBr pellets) were recorded on a PerkinElmer Spectrum BX Series FTIR spectrometer, in the 4000–400 cm^{-1} range, with a 2 cm^{-1} resolution. Thermogravimetric analyses (TG-DTG) were performed under a N_2 flow (100 mL min^{-1}) at a heating rate of 5 K min^{-1} with an EXSTAR Thermo Gravimetric Analyzer Seiko 6200. The latter was coupled with a ThermoStarTM GSD 301T mass spectrometer for mass analysis of the volatile species. The elemental analyses were performed using a Thermo FlashEA 1112 Series CHNS–O elemental analyzer with an accepted tolerance of ±2% on carbon (C), hydrogen (H), nitrogen (N) and sulfur (S). X-ray fluorescence (XRF) qualitative analyses were performed under ambient conditions on powdered samples of **Zr_TCPB_F** and **Zr_TCPB_CF3** using a PANalytical MINIPAL 2 instrument equipped with a sealed X-ray tube having a Cr anode. The generator was set at 30 kV and 3 μA. The nature and purity of all the batches employed for the functional characterization were assessed through powder X-ray diffraction (PXRD). PXRD qualitative measurements were carried out in the 2.0–50.0° 2θ region with a Panalytical X'PERT PRO diffractometer equipped with a Ni filter in the diffracted beam, a PIXcel© solid state detector and a sealed X-ray tube (Cu Kα, λ = 1.5418 Å). Slits were used on both the incident (Soller slits aperture: 0.25°; divergence slit aperture: 0.5°) and the diffracted (anti-scatter slit aperture: 7.5 mm) beam. The generator was operated at 40 kV and 40 mA.

2.2 Synthesis of Zr_TCPB_F

(HPhTz^{F})Br (FW = 318.16, 0.081 g, 0.25 mmol, 5 eq.) was dissolved in 45 mL of anhydrous MeCN : DMSO (9 : 1). **Zr_TCPB** [$Zr_6O_4(OH)_6(H_2O)_2(HCOO)_2(TCPB)_2$, FW = 1948.47, 0.01 g, 0.05 mmol] was added and dispersed in the previous solution under stirring. The mixture was heated at 353 K for 24 h. After cooling, the microcrystalline off-white powder of **Zr_TCPB_F** was collected, washed with hot MeCN (3 × 10 mL) and acetone (3 × 10 mL) and finally dried under a nitrogen stream at room temperature. Yield: 73% (based on the minimal formula [$Zr_6O_4(OH)_5(H_2O)$(**PhTz^{F}**)$(HCOO)_2(TCPB)_2$]Br). Elemental analysis calcd. (%) for **Zr_TCPB_F**, $C_{81}H_{53}FNO_{32}Zr_6BrS$ (MW = 2230.6 g mol^{-1}): C 43.6, H 2.4, N 0.6, S 1.4. Elemental analysis found (%): C, 43.8; H, 2.9; N, 0.7; S, 1.5. IR bands (KBr pellet, cm^{-1}, Fig. S3): 1695(br), 1606(s), 1545(br), 1420(vs), 1183(w), 1146(w), 1108(w), 1018(w), 1004(w), 861(w), 782(m), 740(w), 716(m), 660(br), 582(w), 476(br).

2.3. Synthesis of Zr_TCPB_CF3

(HPhTz^{CF3})Br (FW = 368.17, 0.094 g, 0.26 mmol, 5 eq.) was dissolved in 45 mL of anhydrous MeCN : DMSO (9 : 1). **Zr_TCPB** [$Zr_6O_4(OH)_6(H_2O)_2(HCOO)_2(TCPB)_2$, FW = 1948.47, 0.01 g, 0.05 mmol] was added and dispersed in the previous solution under stirring. The mixture was heated at 353 K for 24 h. After cooling, the microcrystalline off-white powder of **Zr_TCPB_CF3** was collected, washed with hot MeCN (3 × 10 mL) and acetone (3 × 10 mL) and finally dried under a nitrogen stream at room temperature. Yield: 75% (based on the minimal formula [$Zr_6O_4(OH)_5(H_2O)$(**PhTz^{CF3}**)$(HCOO)_2(TCPB)_2$]Br). Elemental analysis calcd. (%) for **Zr_TCPB_CF3**, $C_{82}H_{53}F_3NO_{32}Zr_6BrS$ (MW = 2280.6 g mol^{-1}): C 43.2, H 2.3, N 0.6, S 1.4. Elemental analysis found (%): C, 43.4; H, 2.6; N, 0.6; S, 1.7. IR bands (KBr pellet, cm^{-1}, Fig. S4): 1701(br), 1602(s), 1543(br), 1414(vs), 1308(m), 1288(w), 1122(br), 1054(w), 1020(w), 861(w), 782(m), 714(m), 662(br), 584(br), 478(br).

2.4. Textural properties assessment through N_2 adsorption. CF_4 and SF_6 adsorption isotherms

Due to the thermal instability of the thiazolium salts when encapsulated in **Zr_TCPB** (see the TGA-MS results reported in Fig. S9 and S10), the powdered samples (*ca.* 40 mg) of **Zr_TCPB** and **Zr_TCPB_F/CF3** were activated at T = 423 K and 298 K respectively, under high vacuum (10^{-6} Torr) for 24 h before the measurement. The Brunauer–Emmett–Teller (BET) specific surface area, pore size distribution and pore volume (V_{tot}, V_{micro}) were estimated by volumetric adsorption with an ASAP 2020 Micromeritics® instrument, using N_2 as adsorbate at T = 77 K. For the BET specific surface area calculation, the 0.01–0.1 p/p_0 pressure range of the isotherm was used to fit the data. Within this range, all the Rouquerol consistency criteria[38,39] are satisfied. The material (micro)porosity was determined from the N_2 adsorption isotherm using a NLDFT method (Tarazona approximation) and assuming a cylindrical pore shape (typical of metal oxides). SF_6 and CF_4 adsorption isotherms were recorded at T = 273 K, 298 K and 323 K at a maximum pressure of 1.2 bar, while the N_2 adsorption isotherms used for the selectivity calculations were collected at T = 298 K at a maximum pressure of 1.2 bar. The isosteric heat of adsorption (Q_{st}) values of both gases were calculated from the three isotherms at the lowest comparable coverage according to the differential form of the Clausius–Clapeyron equation:[40,41]

$$\left[\frac{\partial(\ln p)}{\partial\left(\frac{1}{T}\right)}\right]_{\theta} = -\frac{Q_{st}}{R} \quad (1)$$

where R is the gas constant (8.314 J K^{-1} mol^{-1}). The IAST A/B adsorption selectivity (A, B = SF_6, CF_4, N_2) of binary mixtures at a total pressure of 1 bar[42] and at T = 298 K was determined as the ratio of the adsorbed molar fractions of the two gases divided by the ratio of the gas phase initial molar fractions:[43]

$$S_{A/B} = \frac{\left(\frac{\chi_A}{\chi_B}\right)_{ads}}{\left(\frac{\chi_A}{\chi_B}\right)_{gas}} \quad (2)$$

The $(\chi_A)_{ads}$ and $(\chi_B)_{ads}$ values were derived from the application of the free software pyIAST (https://github.com/CorySimon/pyIAST) to the experimental single-component isotherms collected at the chosen temperature. The initial composition (%) selected for the calculation was [50 : 50] for the $[SF_6 : CF_4]$ pair and [5 : 95] for the $[SF_6 : N_2]$ and $[CF_4 : N_2]$ pairs (the latter chosen to have compositions closer to the real atmospheric relative abundances). Various models (Quadratic, BET, Henry) were employed for the SF_6, CF_4 and N_2 isotherms fitting, choosing the option that gives the lowest root-mean-square error (RMSE) on the experimental points (see Table S3 for the list of the fitting parameters). For a detailed explanation of these models and the related parameters, see the pyIAST webpage and documentation.

2.5. Computational details

Periodic DFT calculations were performed at the PBEsol0-3c level of theory,[44] developed by some of us in the CRYSTAL code.[45] PBEsol0-3c is a cost-effective composite method that has been shown to accurately predict structural features[46] and adsorption properties[33,47–49] of MOFs. It is based on the global hybrid PBEsol0 [50,51] exchange–correlation functional combined with a double-zeta quality basis set for solid-state systems, and augmented with the D3 [52] and gCP[53] corrections to account for van der Waals interactions and to remove the basis set superposition error (BSSE), respectively. For the numerical integration of the exchange-correlation term, 75 radial points and 974 angular points (XLGRID) in a Lebedev scheme were adopted. The SCF convergence was set to 10^{-7} during geometry optimization. The Pack–Monkhorst/Gilat shrinking factors for the diagonalization of the Kohn–Sham matrix in reciprocal space were set to 2. The truncation criteria (TOLINTEG) for the bi-electronic integrals (Coulomb and exchange series) were set to 7 7 7 7 25. The JMol[54] software was used to plot the electrostatic potential (ESP) maps.

3 Results and discussion

3.1 Synthesis and characterization of Zr_TCPB_F and Zr_TCPB_CF3

With the aim of preparing functional MOFs with fluorinated groups through extra linker insertion, we chose to start from the 8-coordinated zirconium MOF built with the commercially available tetradentate linker 1,2,4,5-tetrakis(4-carboxyphenyl)benzene: **Zr_TCPB**. This MOF has already been reported in the literature by the groups of Stock (with the label Zr-CAU-24) and Farha (called NU-903) in 2016 [55] and 2019,[37] respectively. It is a porous framework with rhombic channels of approximately 5.3 × 10.5 Å, suitable for hosting additional linkers of small–medium size. With this in mind and following the same approach used in the past for the synthesis of MOF linkers through N-quaternization of thiazole rings,[35,36] we designed two new monocarboxylic fluorinated linkers using the F-containing molecules 4-(bromomethyl)-3-fluorobenzoic acid and 4-(bromomethyl)-3-(trifluoromethyl) benzoic acid (see the SI). The molecular size of [**(HPhTz^{F})Br**] (8.8 Å) and [**(HPhTz^{CF3})Br**] (9.0 Å) estimated from their crystal structures perfectly fits with the channel dimensions of **Zr_TCPB**. Thus, the MIXMOFs **Zr_TCPB_F** and **Zr_TCPB_CF3** preparation was attempted through a post-synthetic SALI functionalization, *i.e.* a condensation reaction between the –COOH group of the thiazolium salts and the OH/H_2O groups on the defects of the 8-coordinated $[Zr_6]$ metallic nodes. The pristine MOF was suspended in an anhydrous MeCN/DMSO mixture containing the dissolved salts and kept at $T = 353$ K for 24 h under gentle stirring. Subsequent filtration and washing with hot MeCN/acetone led to the successful obtainement of the pure products. **Zr_TCPB_F** and **Zr_TCPB_CF3** have been thoroughly characterized in the solid state. The IR spectroscopic analysis confirms the extra-ligand insertion (Fig. S3 and S4), highlighting some typical bands of **(HPhTz^{F})Br**/**(HPhTz^{CF3})Br** at 1695/1701 cm^{-1} [ν(COO)], 1545/1543 cm^{-1} [ν(C=C)], 1420/1414 cm^{-1} [δ(CH/CH_2)], 1183/1308 cm^{-1} [ν(Ar–F)/$\nu(CF_3)$] and 861/860 [γ(C–H)] respectively, besides those of $TCPB^{4-}$ at 1605/1601 cm^{-1} [ν(COO)]. The XRF qualitative analysis (Fig. S5 and S6) highlighted the presence of sulphur and bromine, confirming the successful SALI functionalization and revealing that the **(HPhTz^{F})Br** and **(HPhTz^{CF3})Br** ligands are incorporated within the MOF in their deprotonated form; the bromide anion is then necessary to balance the overall framework charge. Powder X-ray diffraction (PXRD, Fig. 1a) confirms that the parent crystallographic symmetry (orthorhombic, space group *Cmmm*)[37] and network structural motif remain unaltered after functionalization. Differences in diffraction peaks relative intensities are due to changes in the electron density distribution introduced by the thiazolium salts within the unit cell. The extra-ligand is very likely to replace one OH/H_2O couple on the metal node and not a bridging formate, given the favourite entropic factor associated to this coordination mode and the higher acidity of formic acid ($pK_a = 3.75$) compared to benzoic acid ($pK_a = 4.19$) that prevents a formate/benzoate exchange. This hypothesis is also supported by the presence of formic acid (m/z = 45 a.m.u.) in the mass spectra of the volatile byproducts forming during the MOFs thermal decomposition (*vide infra*). Therefore, this model structure has also been taken as starting guess for the DFT analysis (§3.4). To further support our structural hypothesis, a comparison between the experimental PXRD pattern and a "computational" pattern derived from the DFT-optimized model structures of **Zr_TCPB_F** and **Zr_TCPB_CF3** has been made (Fig. S7 and S8). The matching between experimental and theoretical pattern is quite satisfactory. In the latter, there are more peaks coming from the lower crystal symmetry of the DFT model in comparison with that of the real crystal, because in the model there is only a finite portion of the lattice. This symmetry decrease generates additional peaks that are absent in the real sample. Since both **(HPhTz^{F})Br** and **(HPhTz^{CF3})Br** are unstable under strongly acidic or basic conditions (but –F/–CF_3 signals remain detectable), linker quantification was carried out through combined ^{1}H and ^{19}F NMR spectroscopy of the digested solid in

acidic solution (D_2SO_4). See the SI and Fig. S9–S12 for details. ^{19}F signals are integrated against the ^{1}H NMR signals of the H_4TCPB ligand using 2,6-difluorobenzoic acid an internal standard.[56] The multinuclear NMR analysis accounts for one thiazolium salt molecule per minimal formula, in line with the estimation coming from the S-elemental analysis (Experimental section). Consequently, based on the ligands relative stoichiometric ratio the MOF minimal formulae can be written as $[Zr_6O_4(OH)_5(H_2O)(HCOO)_2(TCPB)_2(\mathbf{PhTz^F})]Br$ and $[Zr_6O_4(OH)_5(H_2O)(HCOO)_2(TCPB)_2(\mathbf{PhTz^{CF3}})]Br$. Thermogravimetric analysis (TGA, Fig. S13a and S14a) showed that the thermal stability of both MIXMOFs is lower than that of parent **Zr_TCPB** (T_{dec} = 773/798 *vs.* 820 K for **Zr_TCPB_F**/**Zr_TCPB_CF3** *vs.* **Zr_TCPB**, respectively). An initial weight loss of *ca.* 18–20 wt% (in line with the stoichiometric 1 : 1 [Zr_6] : thiazolium salt ratio) can be reasonably ascribed to loss of the salt and formic acid. Indeed, the DTG peaks found in this range fall at T = 429 K (salt) and T = 543 K (HCOOH). The former temperature value is close to that found for the decomposition of the isolated **(HPhTz^F)Br** and **(HPhTz^{CF3})Br**, occurring at T = 495 and 530 K, respectively (Fig. S15). Further proof of evidence is provided by the MS analysis of the volatiles (Fig. S13b and S14b), where two peaks at m/z = 85 and 46 a.m.u. typical of thiazole and formic acid appear in the same temperature range. MOF decomposition is witnessed by the presence in the MS spectra of the volatiles of the peak at m/z = 78 a.m.u. typical of phenyl rings coming from TCPB.

3.2. Textural properties assessment. CF_4 and SF_6 adsorption isotherms

The porosity of **Zr_TCPB_F**/**Zr_TCPB_CF3** was evaluated through volumetric N_2 adsorption at T = 77 K on pre-activated samples (Fig. 1b). The isotherm shape of Type I is the same as that of **Zr_TCPB**, typical of microporous materials. The BET surface area (1141/1126 *vs.* 1406 $m^2\ g^{-1}$ for **Zr_TCPB_F**/**Zr_TCPB_CF3** *vs.* **Zr_TCPB**, respectively) as well as the total pore volume (0.53/0.46 *vs.* 1.60 $cm^3\ g^{-1}$ for **Zr_TCPB_F**/**Zr_TCPB_CF3** *vs.* **Zr_TCPB**, respectively) are lower than that of pristine **Zr_TCPB**. This is in line with a partial micropore filling by the added thiazolium salts and of the successful SALI functionalization. Additional proof of evidence comes from the DFT pore size distribution (Fig. S16): the two main micropore sizes centered at w = 13.5 and 14.5 Å present in pristine **Zr_TCPB** partially disappear after the extra-linker inclusion in **Zr_TCPB_F** (main micropore diameter w = 13.5 Å only) and **Zr_TCPB_CF3** (main micropore diameter w = 14.7 Å only). The BET area values found in our samples are comparable to those reported for similar MOFs in the literature bearing variably substituted TCPB linkers combined with [Zr_6] metal nodes, such as NU-1008 (linker TCPB-Br_2; BET area = 1370 $m^2\ g^{-1}$),[57] NU-600 (linker TCPB-Br_2; BET area = 1490 $m^2\ g^{-1}$), NU-603 (linkers TCPB-Br_2 and BDC; BET area = 1300 $m^2\ g^{-1}$), NU-604 (linkers TCPB-Br_2 and BPDC; BET area = 1300 $m^2\ g^{-1}$), NU-605 (linkers TCPB-Br_2, BDC and BPDC; BET area = 1280 $m^2\ g^{-1}$),[58] NU-904 (linker TCPB-NO_2; BET area = 1410 $m^2\ g^{-1}$).[37] The activated materials have been tested in SF_6 and CF_4 adsorption at p_{max} = 1.2 bar and at variable temperatures: T = 273, 298 and 323 K (Fig. S17 and S18). Both **Zr_TCPB_F** and **Zr_TCPB_CF3** showed an increased affinity for both gases if compared with their parent MOF **Zr_TCPB**. The total SF_6 uptake at p_{SF6} = 1 bar and T = 298 K is 32.8 wt% (2.2 mmol g^{-1}) and 37.1 wt% (2.5 mmol g^{-1}) for **Zr_TCPB_F** and **Zr_TCPB_CF3**, respectively (Fig. 2a). The absolute gas uptake at ambient temperature is proportional to the material surface area and it is much higher than that found for other Zr-based MOFs of the literature with smaller pore size like UiO-66 (1.6 mmol g^{-1}) and UiO-66-Br_2 (0.9 mmol g^{-1}),[59] but it is lower than that of UiO-67 (4.0 mmol g^{-1}).[60] In terms of SF_6 isosteric heat of adsorption at zero coverage (Q_{st}), the thiazolium-functionalized MOFs are featured by a higher Q_{st} value than that found for its parent analogue (27.5/27.0 *vs.* 24.9 kJ mol^{-1} for **Zr_TCPB_F**/**Zr_TCPB_CF3** *vs.* **Zr_TCPB**,

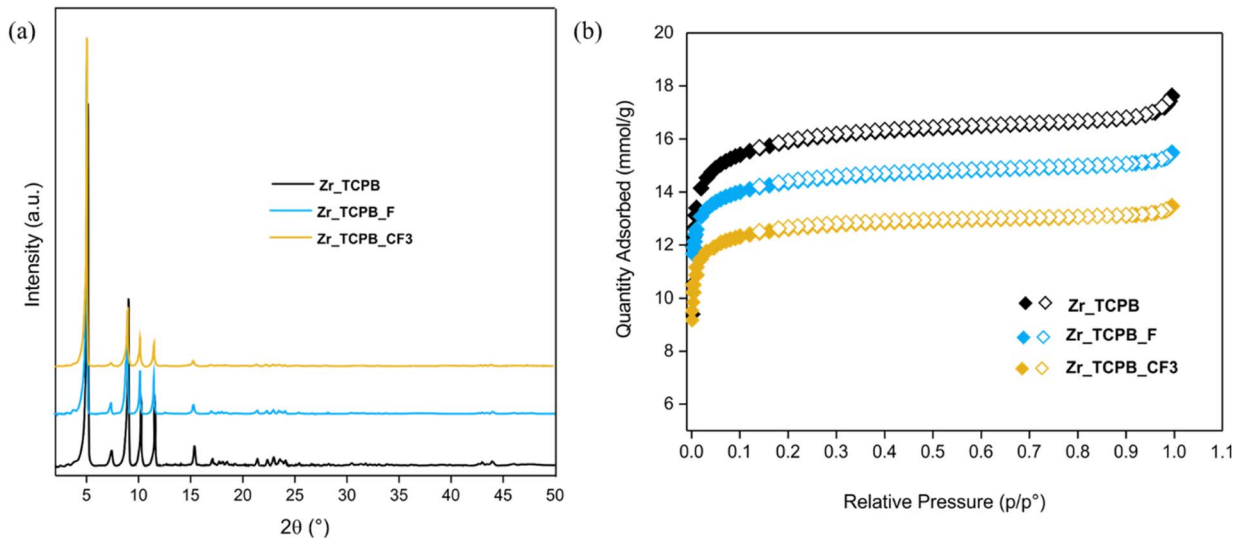

Fig. 1 (a) PXRD patterns (2–50° 2θ region) of **Zr_TCPB**, **Zr_TCPB_F** and **Zr_TCPB_CF3** at comparison. (b) N_2 isotherms measured at T = 77 K on thermally activated **Zr_TCPB**, **Zr_TCPB_F** and **Zr_TCPB_CF3** at comparison. Empty symbols denote the desorption branch.

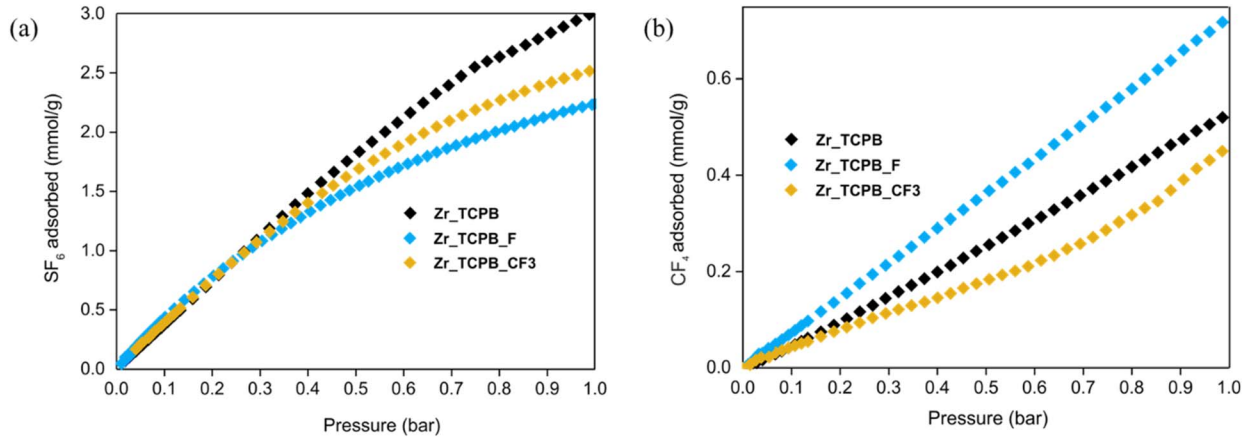

Fig. 2 Collective (a) SF_6 and (b) CF_4 adsorption isotherms at $T = 298$ K for **Zr_TCPB**, **Zr_TCPB_F** and **Zr_TCPB_CF3** in comparison. The corresponding graphs for $T = 273$ K and $T = 323$ K are reported in Fig. S17 and S18, respectively.

respectively, Table 1, Fig. S19 and S20). This is a proof of evidence that the SALI functionalization is beneficial for the improvement of the material thermodynamic affinity for sulfur hexafluoride. SF_6 adsorption at low pressures can be greatly improved by incorporating a fluorinated functional group with a high polarizability into the pores of the adsorbent; the introduction of a polar molecule like a fluorinated thiazolium salt into the MOF channels strengthens the MOF–SF_6 interaction. However, in comparison with other Zr-based MOFs of the literature (Table S4), the absolute Q_{st} (SF_6) values of **Zr_TCPB_F** and **Zr_TCPB_CF3** are lower than those of the UiO-66-X (X = NH_2, NO_2, Cl, Br, Br, I) family (between 32 and 45 kJ mol^{-1})[59] but they are higher than that of UiO-67 (20 kJ mol^{-1}).[60] This may be due to the stronger host-guest interaction occurring in smaller pores. Widening the horizon to non-Zr-based MOFs, the values found in our samples are comparable to those of MIL-100(Fe) (2.7 mmol g^{-1}) or DUT-9 (2.1 mmol g^{-1}), but they are lower than that of HKUST-1 with Cu^{II} open metal sites (4.0 mmol g^{-1}).[25] As for CF_4, the total gas uptake at $p_{CF4} = 1$ bar and $T = 298$ K is 6.5 wt% (0.7 mmol g^{-1}) and 4.1 wt% (0.5 mmol g^{-1}) for **Zr_TCPB_F** and **Zr_TCPB_CF3**, respectively (Fig. 2b). The quantities adsorbed are smaller than those of SF_6 under the same temperature and pressure conditions, and they are again proportional to the surface areas. The values found in our samples are comparable to those found for the UiO-66-X (X = NH_2, NO_2, Cl, Br, Br, I) family (between 0.5 and 0.7 mmol g^{-1}, Table S4).[59] If we consider other non-Zr-based MOFs, the amount of CF_4 adsorbed by **Zr_TCPB_F** in particular is comparable to that of HKUST-1 (1.0 mmol g^{-1}),[25] despite the absence of open metal sites in the former. As observed for SF_6, the CF_4 isosteric heats of adsorption at zero coverage of both **Zr_TCPB_F** and **Zr_TCPB_CF3** are higher than that of bare **Zr_TCPB** (22.1/30.1 *vs.* 21.9 kJ mol^{-1} for **Zr_TCPB_F**/**Zr_TCPB_CF3** *vs.* **Zr_TCPB**, respectively, Table 1, Fig. S19 and S20), showing again the beneficial effect coming from the inclusion of the fluorinated linker in the pores. Interestingly, a simple modification of the fluorinated group in the thiazolium salt induces a switch in the thermodynamic affinity for the two gases: while the fluoro substituent in **Zr_TCPB_F** gives a material where Q_{st} (SF_6) > Q_{st} (CF_4), the opposite holds for the trifluoromethyl group in **Zr_TCPB_CF3**, where Q_{st} (SF_6) < Q_{st} (CF_4). Therefore, these MOFs may represent "smart materials" for the discrimination of fluorinated polluting gases, opening new horizons in the field of air treatment and cleaning. In order to validate the suitability of these materials for practical use in real life contexts, long-term cycling stability tests were carried out with **Zr_TCPB_F** and SF_6 at ambient temperature (Fig. S21). The amount of gas adsorbed is constant after four repeated adsorption/desorption cycles on the same batch (briefly reactivated under high vacuum for 2 h each time before the next cycle), confirming the MOF stability under these conditions. To shed further light on the MOFs adsorption behavior, IAST selectivity ($S_{SF6/CF4}$) data for [SF_6/CF_4] binary equimolar mixtures at $T = 298$ K were estimated; the results are summarized in Table 2. Despite their different Q_{st} values, all the three samples examined in this study show a preferential adsorption for sulfur hexafluoride. Albeit it is difficult to provide a comprehensive explanation of this phenomenon, the reason

Table 1 Main adsorption data for the MOFs in this study

Sample	BET area [m^2 g^{-1}]	Q_{st} (CF_4) [kJ mol^{-1}]	CF_4 quantity adsorbed at $T = 298$ K, $p = 1$ bar [mmol g^{-1}]	Q_{st} (SF_6) [kJ mol^{-1}]	SF_6 quantity adsorbed at $T = 298$ K, $p = 1$ bar [mmol g^{-1}]
Zr_TCPB	1406	21.9	0.54 (4.7 wt%)	24.9	3.04 (44.4 wt%)
Zr_TCPB_F	1141	22.1	0.73 (6.5 wt%)	27.5	2.24 (32.8 wt%)
Zr_TCPB_CF3	1126	30.1	0.47 (4.1 wt%)	27.0	2.54 (37.1 wt%)

Table 2 IAST SF_6/CF_4 adsorption selectivity data of binary gas mixtures [50%:50%], SF_6/N_2 and CF_4/N_2 adsorption selectivity data of binary gas mixtures [5%:95%] at $p_{tot} = 1$ bar and $T = 298$ K for **Zr_TCPB**, **Zr_TCPB_F** and **Zr_TCPB_CF3**

MOF	S_{SF_6/CF_4}	S_{SF_6/N_2}	S_{CF_4/N_2}
Zr_TCPB	6	25	4
Zr_TCPB_F	5	42	7
Zr_TCPB_CF3	9	38	3

may stem from the different polarizability of the two gases. Both CF_4 and SF_6 are globally nonpolar, but for slightly different reasons. C–F and S–F are both highly polarized bonds due to the high electronegativity of fluorine. The tetrahedral/octahedral molecular symmetry causes these dipoles to cancel each other out. However, SF_6 has a higher polarizability (due to the much larger and more diffuse central sulfur atom) that translates into stronger dispersion (van der Waals) interactions with the MOFs. On the other hand, CF_4 is less polarizable, more volatile and less easily adsorbed. The analysis of the SF_6/CF_4 adsorption selectivity and the possibility to discriminate between SF_6 and CF_4 through tailored (fluorinated) MOFs is unprecedented to our knowledge, and even more unexpected given the identical C–F and S–F bond polarization (based on the elements electronegativity: 2.5 and 4.0 for both C/S and F, respectively) and taking into account the considerations outlined in the previous paragraph. $S_{SF6/CF4}$ reaches its maximum value (9) in **Zr_TCPB_CF3**. While the presence of the fluoro-substituent does not modify the selectivity significantly, a better improvement is observed upon introduction of the trifluoromethyl group. As for the selectivity towards N_2, all MOFs show a preferential adsorption for the fluorinated gases (for SF_6 in particular), given the extremely low amount of N_2 adsorbed at ambient temperature (Fig. S22) even from highly nitrogen-enriched mixtures as that taken into account for the selectivity calculation [95%(N_2): 5-%(fluorinated gas)], more representative of the real atmospheric composition (the current concentration of CF_4 and SF_6 in the atmosphere is 90–100 ppt and 12 ppt, respectively).

3.3. Dynamic breakthrough experiments with binary SF_6/CF_4 mixtures

Given the promising separation potential, the breakthrough experiment was further implemented at ambient conditions with the binary SF_6/CF_4 gaseous blend (volume ratio 50/50) that mimics the real typical industrial composition. At $T = 298$ K and $p_{tot} = 1$ bar, the SF_6/CF_4 mixture was fed at a flow rate of 2 mL min^{-1} into adsorption columns. The actual separation performance of the adsorbent for the two components is evaluated by monitoring the relative breakthrough times of SF_6 and CF_4. Experimental results demonstrate that both **Zr_TCPB_F** and **Zr_TCPB_CF3** achieve effective separation of SF_6 from CF_4. As displayed in Fig. 3, CF_4 elutes immediately from the breakthrough column at 12.5 min and 10 min for **Zr_TCPB_F** and **Zr_TCPB_CF3**, respectively. In stark contrast, SF_6 exhibits a noticeable breakthrough delay with its elution detected at 25 min for both MOFs, with an experimentally measured residence time difference between the two gases of 12.5 min and 15 min for **Zr_TCPB_F** and **Zr_TCPB_CF3**, respectively.

The separation factors obtained from the breakthrough experiments (Fig. S23 and eqn S3) are 6.66 for **Zr_TCPB_F** and 11.40 for **Zr_TCPB_CF3**, while the calculated IAST SF_6/CF_4 adsorption selectivity equals 5 and 9, respectively (Table 2). Although the experimental separation factors slightly exceed the calculated IAST selectivity values, the overall trend holds true, with **Zr_TCPB_CF3** exhibiting superior separation efficiency. Furthermore, the high purity SF_6 productivity of **Zr_TCPB_CF3** calculated from single separation breakthrough curves is about 1.61 mmol g^{-1}, larger than the 1.53 mmol g^{-1} found for **Zr_TCPB_F** (eqn S1 and S2). This evidence shows that multiple and complex supramolecular interactions are at work when the two MOFs bind SF_6 or CF_4.

3.4. DFT calculation of the electronic structure of Zr_TCPB_F/CF3 and their CF_4/SF_6 adducts

To build a realistic computational model of **Zr_TCPB**, the initial guess structure was taken from the CIF file deposited in the Cambridge Structural Database (CSD) with RefCode IZIBUQ.[55] The Zr atoms of the Inorganic Building Unit (IBU) have been

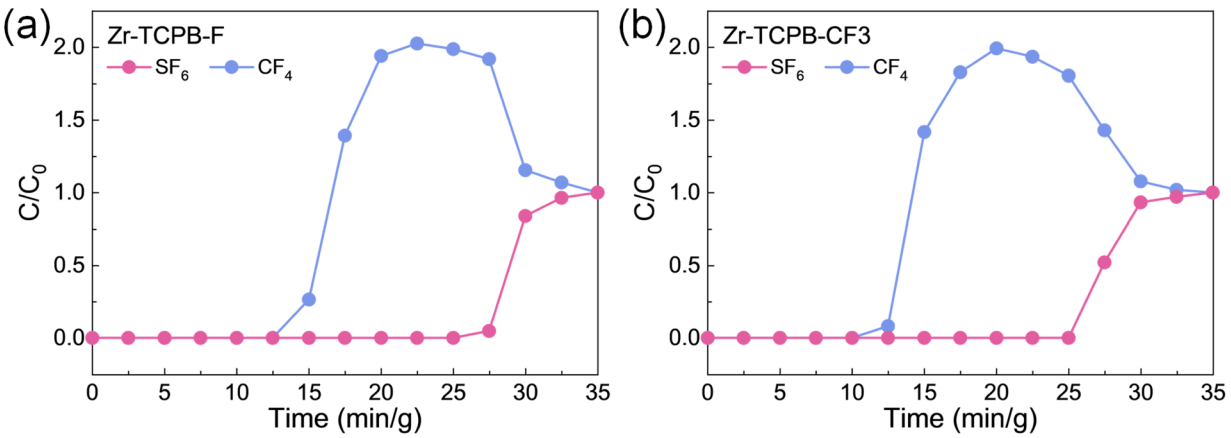

Fig. 3 Breakthrough curves for a binary SF_6/CF_4 (50/50, v/v) mixture: (a) **Zr_TCPB_F** and (b) **Zr_TCPB_CF3**.

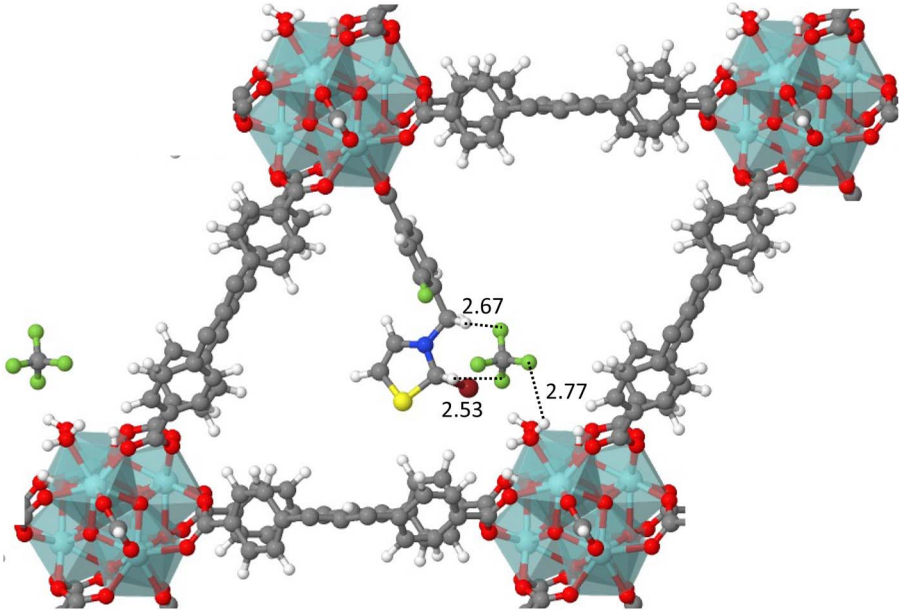

Fig. 4 Optimized geometry of [CF_4@Zr_TCPB_F] (portion of the crystal structure only, for the sake of clarity). Main gas-framework distances reported (Å).

saturated with OH and H_2O to ensure the electroneutrality of the model system. For the **Zr_TCPB_F** and **Zr_TCPB_CF3** models, the thiazolium salts were covalently bound to the inorganic nodes, by removing one H_2O molecule and a OH^- group from the IBU, and a proton (H^+) from the **(HPhTz^{F})Br** and **(HPhTz^{CF3})Br** salts, respectively. First, the atomic positions and lattice parameters of the empty framework models were fully relaxed. Then, to gain insight into the host-guest interactions and to identify the primary CF_4 and SF_6 adsorption sites in the MOFs, the gas molecules were manually docked into the framework pores by maximizing the interactions between host and guest through the complementarity of electrostatic potentials (Fig. S24–S27). In **Zr_TCPB**, CF_4 and SF_6 form hydrogen bonds with OH groups and H_2O molecules of the $[Zr_6(\mu_3\text{-}O)_4(\mu_3\text{-}OH)_4]^{12+}$ node and engage in F···H–C interactions with the $TCPB^{4-}$ linker (Fig. S28 and S29). The same kind of hydrogen bonds were found in **Zr_TCPB_F** and **Zr_TCPB_CF3** where the host-guest assemblies are further characterized by the formation of F···H hydrogen bonds and electrostatic interactions with the thiazolium salts, as shown by the optimized structures

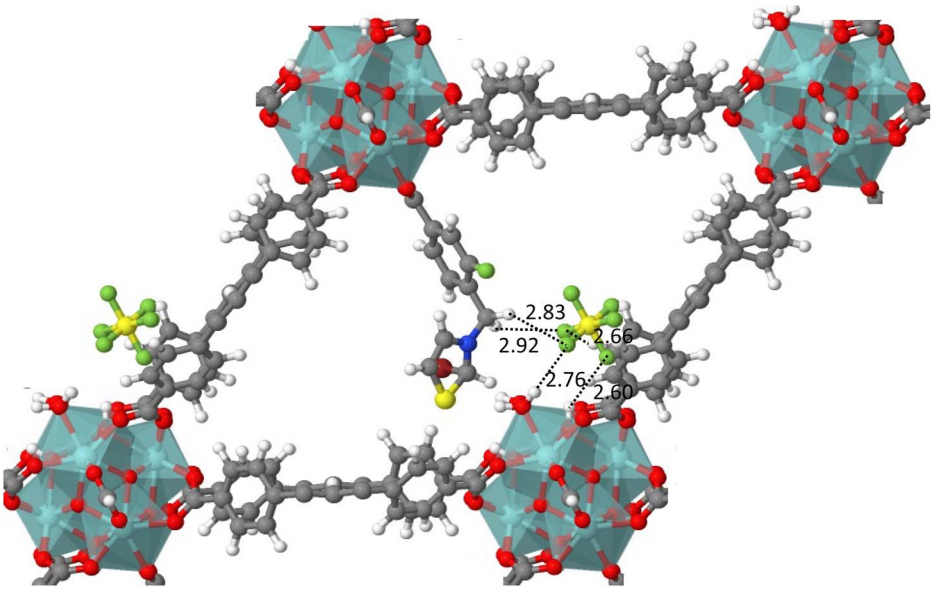

Fig. 5 Optimized geometry of [SF_6@Zr_TCPB_F] (portion of the crystal structure only, for the sake of clarity). Main gas-framework distances reported (Å).

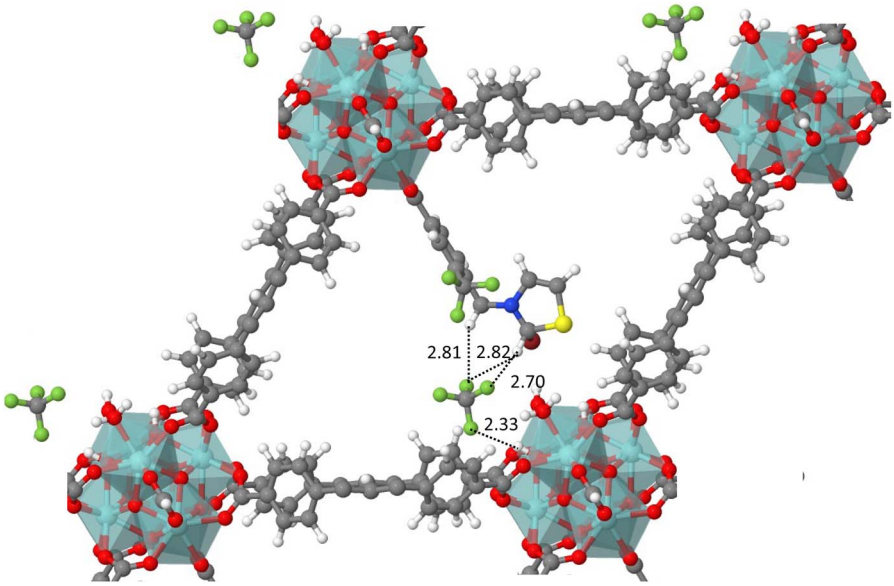

Fig. 6 Optimized geometry of [CF_4@**Zr_TCPB_CF3**] (portion of the crystal structure only, for the sake of clarity). Main gas-framework distances reported (Å).

depicted in Fig. 4 and 5 for **Zr_TCPB_F** and in Fig. 6 and 7 for **Zr_TCPB_CF3**, respectively. Additionally, CF_4 and SF_6 tend to form weak sigma–hole (σ–hole) interactions with the Lewis base groups (H_2O and OH) of the IBU through the polarized central atom. Similar weak interactions were previously reported for the selective adsorption of fluorinated gases in different MOF materials.[22,61–63] Overall, the computed adsorption energies (Tables S5 and S6) are in reasonable agreement with the experimental findings, especially for **Zr_TCPB** and **Zr_TCPB_CF3**, while larger deviations are observed for **Zr_TCPB_F**. This discrepancy can be attributed to the presence of defects, amorphization, or other structural changes present in the real samples that were not accounted for in our "ideal" computational models. Given the limited thermal stability of the thiazolium salts [**(HPhTz^{F})Br**] and [**(HPhTz^{CF3})Br**], the activation of **Zr_TCPB_F** and **Zr_TCPB_CF3** cannot be performed at

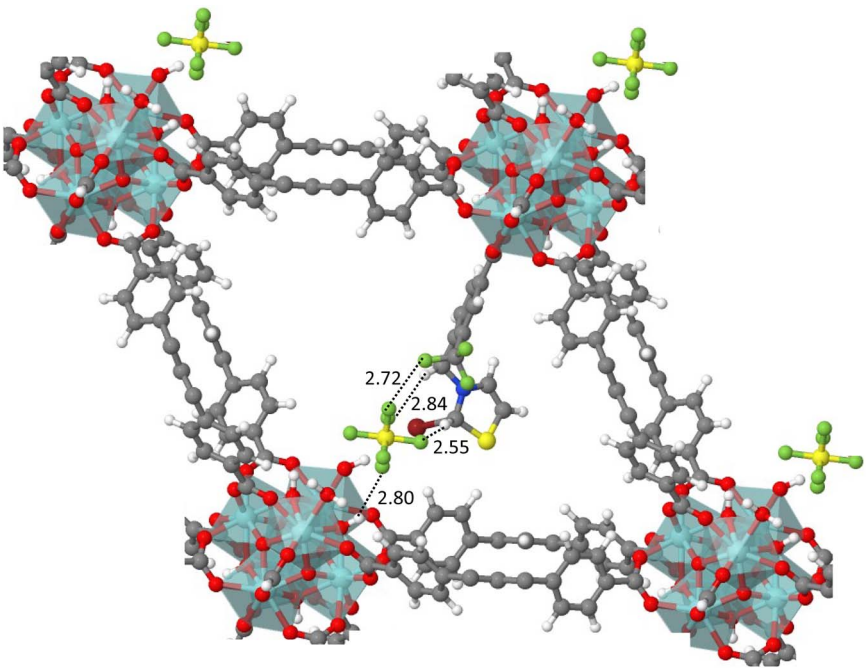

Fig. 7 Optimized geometry of [SF_6@**Zr_TCPB_CF3**] (portion of the crystal structure only, for the sake of clarity). Main gas-framework distances reported (Å).

high temperature. Consequently, some residual solvent may still be present after activation, blocking the gas access to the high-energy adsorption site (presumably close to the metallic node).

4 Conclusions

Following the research interest of our groups in the exploitation of MOFs for gas mixture adsorption and separation, we have prepared two new mixed-linker MOFs **Zr_TCPB_F** and **Zr_TCPB_CF3** *via* SALI starting from the 8-connected zirconium MOF **Zr_TCPB** and decorating it with two fluorinated monocarboxylic thiazolium salts. The solids have been fully characterized in the solid-state and tested as functional materials for SF_6 and CF_4 adsorption. The presence of the F-containing dangling group in the MOFs pores is beneficial for the improvement of their chemical interaction with fluorinated gases, as witnessed by the higher SF_6 and CF_4 adsorption enthalpies of **Zr_TCPB_F** and **Zr_TCPB_CF3** if compared with those of their parent material **Zr_TCPB**. More importantly, the (unprecedented) possibility to switch the MOF preferential adsorption from SF_6 to CF_4 through a simple replacement of the fluoro substituent with a trifluoromethyl group on the thiazolium salt opens promising perspectives for a selective adsorption of fluorinated gases with very similar physico-chemical nature (non-polar molecules) and bond polarity. Consequently, the prepared materials may find application in the field of atmospheric pollution treatment and air cleaning from dangerous gases to mitigate the greenhouse effect and the ozone layer depletion.

Author contributions

G. P., G. B., Z. F., T. Y.: investigation, formal analysis; B. C., G. G., G. T., H. H.: validation; L. D.: investigation, formal analysis, methodology, software, writing – original draft; A. R.: conceptualization, funding acquisition, project administration, supervision, writing – original draft.

Conflicts of interest

The authors have no conflicts of interest to declare.

Data availability

CCDC 2448941 (**HPhTz^{F}**)**Br** and 2448942 (**HPhTz^{CF3}**)**Br** contain the supplementary crystallographic data for this paper.[64a,b]

The data supporting this article have been included as part of the supplementary information (SI). Supplementary information: synthetic procedures and characterization (including crystal structure solution from single-crystal X-ray diffraction) of (**HPhTz^{F}**)**Br** and (**HPhTz^{CF3}**)**Br**, IR, XRF and TG-MS spectra of **Zr_TCPB_F** and **Zr_TCPB_CF3**, comparison between experimental and DFT-simulated PXRD patterns of **Zr_TCPB_F** and **Zr_TCPB_CF3**, linkers quantification through ^{1}H and ^{19}F NMR spectroscopy of the digested samples, breakthrough experiments details and methods, Clausius–Clapeyron data fitting for Q_{st} calculations, long-term stability tests on repeated adsorption/desorption cycles, additional computational details: electrostatic potential maps, interaction energies, optimized geometries of [CF_4@**Zr_TCPB**] and [SF_6@**Zr_TCPB**]. See DOI: https://doi.org/10.1039/d5ta10343f.

Acknowledgements

A. R. and G. B. would like to acknowledge the Italian Ministry of University and Research (MUR) and the European Union (Next Generation EU) for funding this research activity through the PRIN 2022 project LUMIMOF (2022A3XNWJ) "Wastewater treatment and monitoring with luminescent mixed-linker Metal–Organic Frameworks as chemical sensors and adsorbents of contaminants of emerging concern". A. R. is also grateful to Prof. Simona Galli and Ms. Anna Mauri (Università dell'Insubria, Como, Italy) for help with the XRF data collection and for fruitful crystallographic discussions. L. D. and B. C. gratefully acknowledge the support from the Project CH4.0 under the MUR program "Dipartimenti di Eccellenza 2023–2027" (CUP: D13C22003520001).

References

1 D. J. Sheldon and M. R. Crimmin, *Chem. Soc. Rev.*, 2022, **51**, 4977–4995.
2 https://www.ipcc.ch/sr15/chapter/chapter-2/, last access: December 2025.
3 https://www.epa.gov/ghgemissions/fluorinated-gas-emissions, last access: December 2025.
4 J. Kim, R. Thompson, H. Park, S. Bogle, J. Mühle, M.-K. Park, Y. Kim, C. M. Harth, P. K. Salameh, R. Schmidt, D. Ottinger, S. Park and R. F. Weiss, *J. Geophys. Res.:Atmos.*, 2021, **126**, e2021JD034888.
5 D. Say, A. J. Manning, L. M. Western, D. Young, A. Wisher, M. Rigby, S. Reimann, M. K. Vollmer, M. Maione, J. Arduini, P. B. Krummel, J. Mühle, C. M. Harth, B. Evans, R. F. Weiss, R. G. Prinn and S. O'Doherty, *Atmos. Chem. Phys.*, 2021, **21**, 2149–2164.
6 R. H. Harrison and D. R. Douslin, *J. Chem. Eng. Data*, 1966, **11**, 383–388.
7 C. T. Dervos and P. Vassiliou, *J. Air Waste Manage. Assoc.*, 2000, **50**, 137–141.
8 H. C. Miller, L. S. Verdelli and J. F. Gall, *Ind. Eng. Chem.*, 1951, **43**, 1126–1129.
9 W. C. Schumb and E. L. Gamble, *J. Am. Chem. Soc.*, 1930, **52**, 4302–4308.
10 https://www.un.org/en/climatechange/paris-agreement, last access: December 2025.
11 O. M. Yaghi, M. J. Kalmutzki and C. S. Diercks, *Introduction to Reticular Chemistry: Metal–Organic Frameworks and Covalent Organic Frameworks*, Wiley-VCH Verlag GmbH & Co. KGaA, 2019.
12 H. García and S. Navalón, *Metal–Organic Frameworks: Applications in Separations and Catalysis*, ed. H. García and S. Navalón, Wiley-VCH Verlag GmbH & Co. KGaA, 2018.

13 S. Kaskel, *The Chemistry of Metal–Organic Frameworks: Synthesis, Characterization, and Applications*, ed. S. Kaskel, Wiley-VCH Verlag GmbH & Co. KGaA, 2016.
14 D. Farrusseng, *Metal–Organic Frameworks: Applications from Catalysis to Gas Storage*, Wiley-VCH Verlag, Weinheim, 2011.
15 X. Sun, L. Zhou, J. Chen, Z. Jia, Z. Zhao and Z. Zhao, *J. Mater. Chem. A*, 2025, **13**, 2360–2377.
16 E. Jo, S. Yang, D. W. Kim and D. W. Kang, *Coord. Chem. Rev.*, 2024, **515**, 215958.
17 H. Demir and S. Keskin, *Mol. Syst. Des. Eng.*, 2022, **7**, 1707–1721.
18 D. K. J. A. Wanigarathna, J. Gao and B. Liu, *Mater. Adv.*, 2020, **1**, 310–320.
19 G. Xu, T. Ke, R. Fan, K. Tan, W. Zhang, B. Su, Z. Zhang, Z. Bao, Q. Ren and Q. Yang, *Adv. Sci.*, 2025, **12**, 2411083.
20 J. Zhu, J. Hu, H. Xiao, L. Yang, M. Yang, S. Wang, J. Zhang and H. Xing, *Sep. Purif. Technol.*, 2024, **331**, 125614.
21 Z. Wan, T. Yan, M. Chang, M. Yang and D. Liu, *Sep. Purif. Technol.*, 2023, **306**, 122617.
22 S.-M. Wang, H.-L. Lan, G.-W. Guan and Q.-Y. Yang, *ACS Appl. Mater. Interfaces*, 2022, **14**, 40072–40081.
23 M. Chang, T. Yan, Y. Wei, J.-X. Wang, D. Liu and J.-F. Chen, *Chem. Mater.*, 2022, **34**, 9134–9143.
24 T.-H. Chen, I. Popov, W. Kaveevivitchai, Y.-C. Chuang, Y.-S. Chen, A. J. Jacobson and O. Š. Miljanić, *Angew. Chem., Int. Ed.*, 2015, **54**, 13902–13906.
25 I. Senkovska, E. Barea, J. A. R. Navarro and S. Kaskel, *Microporous Mesoporous Mater.*, 2012, **156**, 115–120.
26 S.-M. Wang, P. Duan and Q.-Y. Yang, *Coord. Chem. Rev.*, 2025, **525**, 216339.
27 D. Morelli Venturi and F. Costantino, *RSC Adv.*, 2023, **13**, 29215–29230.
28 A. Ebadi Amooghin, H. Sanaeepur, R. Luque, H. Garcia and B. Chen, *Chem. Soc. Rev.*, 2022, **51**, 7427–7508.
29 T. Islamoglu, S. Goswami, Z. Li, A. J. Howarth, O. K. Farha and J. T. Hupp, *Acc. Chem. Res.*, 2017, **50**, 805–813.
30 P. Deria, W. Bury, I. Hod, C.-W. Kung, O. Karagiaridi, J. T. Hupp and O. K. Farha, *Inorg. Chem.*, 2015, **54**, 2185–2192.
31 P. Deria, W. Bury, J. T. Hupp and O. K. Farha, *Chem. Commun.*, 2014, **50**, 1965–1968.
32 P. Deria, J. E. Mondloch, O. Karagiaridi, W. Bury, J. T. Hupp and O. K. Farha, *Chem. Soc. Rev.*, 2014, **43**, 5896–5912.
33 G. Provinciali, A. L. Capodilupo, A. Mauri, S. Galli, L. Donà, B. Civalleri, G. Tuci, G. Giambastiani, C. Piccirillo and A. Rossin, *ACS EST Water*, 2024, **4**, 2339–2351.
34 G. Mercuri, M. Moroni, S. Galli, C. Piccirillo, A.-L. Capodilupo, G. Tuci, G. Giambastiani and A. Rossin, *Inorg. Chem. Front.*, 2022, **9**, 90–102.
35 G. Mercuri, M. Moroni, S. Galli, G. Tuci, G. Giambastiani, T. Yan, D. Liu and A. Rossin, *ACS Appl. Mater. Interfaces*, 2021, **13**, 58982–58993.
36 L. Luconi, G. Mercuri, T. Islamoglu, A. Fermi, G. Bergamini, G. Giambastiani and A. Rossin, *J. Mater. Chem. C*, 2020, **8**, 7492–7500.
37 J. Lyu, X. Zhang, K.-i. Otake, X. Wang, P. Li, Z. Li, Z. Chen, Y. Zhang, M. C. Wasson, Y. Yang, P. Bai, X. Guo, T. Islamoglu and O. K. Farha, *Chem. Sci.*, 2019, **10**, 1186–1192.
38 D. A. Gómez-Gualdrón, P. Z. Moghadam, J. T. Hupp, O. K. Farha and R. Q. Snurr, *J. Am. Chem. Soc.*, 2016, **138**, 215–224.
39 J. Rouquerol, P. Llewellyn and F. Rouquerol, in *Studies in Surface Science and Catalysis*, ed. P. L. Llewellyn, F. Rodriquez-Reinoso, J. Rouquerol and N. Seaton, Elsevier, Amsterdam, 2007, vol. 160, p. 49.
40 X. Zhu, C. Tian, G. M. Veith, C. W. Abney, J. Dehaudt and S. Dai, *J. Am. Chem. Soc.*, 2016, **138**, 11497–11500.
41 X. Zhu, S. M. Mahurin, S.-H. An, C.-L. Do-Thanh, C. Tian, Y. Li, L. W. Gill, E. W. Hagaman, Z. Bian, J.-H. Zhou, J. Hu, H. Liu and S. Dai, *Chem. Commun.*, 2014, **50**, 7933–7936.
42 The total pressure value of 1 atm has been *arbitrarily* chosen for the sake of simplicity in the IAST calculations, since the $S_{A/B}$ values are only dependent from the mixture composition but not from its total pressure.
43 J. Schell, N. Casas, R. Pini and M. Mazzotti, *Adsorption*, 2012, **18**, 49–65.
44 L. Doná, J. G. Brandenburg and B. Civalleri, *J. Chem. Phys.*, 2019, **151**, 121101.
45 A. Erba, J. K. Desmarais, S. Casassa, B. Civalleri, L. Donà, I. J. Bush, B. Searle, L. Maschio, L. Edith-Daga, A. Cossard, C. Ribaldone, E. Ascrizzi, N. L. Marana, J.-P. Flament and B. Kirtman, *J. Chem. Theory Comput.*, 2023, **19**, 6891–6932.
46 L. Donà, J. G. Brandenburg and B. Civalleri, *J. Chem. Phys.*, 2022, **156**, 094706.
47 M. Pugliesi, M. Cavallo, C. Atzori, B. Garetto, E. Borfecchia, L. Donà, B. Civalleri, G. Tuci, G. Giambastiani, S. Galli, F. Bonino and A. Rossin, *Adv. Funct. Mater.*, 2024, **34**, 2403017.
48 T. Xiong, Y. Zhang, L. Donà, M. Gutiérrez, A. F. Möslein, A. S. Babal, N. Amin, B. Civalleri and J.-C. Tan, *ACS Appl. Nano Mater.*, 2021, **4**, 10321–10333.
49 B. E. Souza, L. Donà, K. Titov, P. Bruzzese, Z. Zeng, Y. Zhang, A. S. Babal, A. F. Möslein, M. D. Frogley, M. Wolna, G. Cinque, B. Civalleri and J.-C. Tan, *ACS Appl. Mater. Interfaces*, 2020, **12**, 5147–5156.
50 J. P. Perdew, A. Ruzsinszky, G. I. Csonka, O. A. Vydrov, G. E. Scuseria, L. A. Constantin, X. Zhou and K. Burke, *Phys. Rev. Lett.*, 2008, **100**, 136406.
51 C. Adamo and V. Barone, *J. Chem. Phys.*, 1999, **110**, 6158–6170.
52 S. Grimme, S. Ehrlich and L. Goerigk, *J. Comput. Chem.*, 2011, **32**, 1456–1465.
53 H. Kruse and S. Grimme, *J. Chem. Phys.*, 2012, 136.
54 R. M. Hanson and X.-J. Lu, *Nucleic Acids Res.*, 2017, **45**, W528–W533.
55 M. Lammert, H. Reinsch, C. A. Murray, M. T. Wharmby, H. Terraschke and N. Stock, *Dalton Trans.*, 2016, **45**, 18822–18826.
56 P. Deria, J. E. Mondloch, E. Tylianakis, P. Ghosh, W. Bury, R. Q. Snurr, J. T. Hupp and O. K. Farha, *J. Am. Chem. Soc.*, 2013, **135**, 16801–16804.

57 Y. Chen, S. Ahn, M. R. Mian, X. Wang, Q. Ma, F. A. Son, L. Yang, K. Ma, X. Zhang, J. M. Notestein and O. K. Farha, *J. Am. Chem. Soc.*, 2022, **144**, 3554–3563.
58 Y. Chen, K. B. Idrees, M. R. Mian, F. A. Son, C. Zhang, X. Wang and O. K. Farha, *J. Am. Chem. Soc.*, 2023, **145**, 3055–3063.
59 M.-B. Kim, K.-M. Kim, T.-H. Kim, T.-U. Yoon, E.-J. Kim, J.-H. Kim and Y.-S. Bae, *Chem. Eng. J.*, 2018, **339**, 223–229.
60 M.-B. Kim, T.-H. Kim, T.-U. Yoon, J. H. Kang, J.-H. Kim and Y.-S. Bae, *J. Ind. Eng. Chem.*, 2020, **84**, 179–184.
61 X. Zhang, Y.-L. Zhao, X.-Y. Li, X. Bai, Q. Chen and J.-R. Li, *J. Am. Chem. Soc.*, 2024, **146**, 19303–19309.
62 M. Zhang, L. Liu, Q. Li, H. Gong and Y. Chen, *Ind. Eng. Chem. Res.*, 2023, **62**, 7103–7113.
63 S.-M. Wang, X.-T. Mu, H.-R. Liu, S.-T. Zheng and Q.-Y. Yang, *Angew. Chem., Int. Ed.*, 2022, **61**, e202207066.
64 (*a*) CCDC 2448941: Experimental Crystal Structure Determination, 2026, DOI: 10.5517/ccdc.csd.cc2n6b3b; (*b*) CCDC 2448942: Experimental Crystal Structure Determination, 2026, DOI: 10.5517/ccdc.csd.cc2n6b4c.